
SPATIALLY SCALABLE RECURSIVE ESTIMATION OF GAUSSIAN PROCESS TERRAIN MAPS USING LOCAL BASIS FUNCTIONS

Frida Marie Viset

Delft Center for Systems and Control
Delft University of Technology
{f.m.viset}@tudelft.nl

Rudy Helmons

Maritime and transport technology
Delft University of Technology
{r.l.j.helmons}@tudelft.nl

Manon Kok

Delft Center for Systems and Control
Delft University of Technology
{m.kok-1}@tudelft.nl

ABSTRACT

When an agent, person, vehicle or robot is moving through an unknown environment without GNSS signals, online mapping of nonlinear terrains can be used to improve position estimates when the agent returns to a previously mapped area. Mapping algorithms using online Gaussian process (GP) regression are commonly integrated in algorithms for simultaneous localisation and mapping (SLAM). However, GP mapping algorithms have increasing computational demands as the mapped area expands relative to spatial field variations. This is due to the need for estimating an increasing amount of map parameters as the area of the map grows. Contrary to this, we propose a recursive GP mapping estimation algorithm which uses local basis functions in an information filter to achieve spatial scalability. Our proposed approximation employs a global grid of finite support basis functions but restricts computations to a localized subset around each prediction point. As our proposed algorithm is recursive, it can naturally be incorporated into existing algorithms that uses Gaussian process maps for SLAM. Incorporating our proposed algorithm into an extended Kalman filter (EKF) for magnetic field SLAM reduces the overall computational complexity of the algorithm. We show experimentally that our algorithm is faster than existing methods when the mapped area is large and the map is based on many measurements, both for recursive mapping tasks and for magnetic field SLAM.

Navigation in large, unknown, nonlinear geospatial fields can be done through simultaneous localisation and mapping (SLAM). This requires a spatially scalable online mapping technique. SLAM using nonlinear geospatial field maps has been used to compensate for odometry drift in robots, marine vehicles, aerial vehicles, and pedestrians [1, 2, 3, 4]. Some nonlinear fields that have been used in SLAM are magnetic fields [4, 5, 1], underwater bathymetry [2, 6], and terrain fields [7, 8]. A range of this research uses Gaussian process (GP) regression [9] to create nonlinear field maps [4, 2, 6, 7, 8]. These methods suffer from the computational complexity scaling either with the number of measurements used to build the map or with the area of the map. To remedy this, we propose a temporally and spatially scalable online GP mapping algorithm that removes this bottleneck from SLAM algorithms that use GPs for terrain navigation. Our proposed approximation uses a global grid of finite-support basis functions to approximate the GP. At each timestep, our approach restricts computations to a local grid of basis functions surrounding each prediction point, as illustrated in Fig. 1, which results in a reduction in computational cost. Our algorithm does not only reduce the computational cost for constructing maps, its recursive nature also opens up for using it in SLAM. We extend the magnetic field SLAM algorithm from [10] to include our recursive mapping algorithm, and show that it causes a reduction in the overall computational complexity of the SLAM algorithm. The magnetic field SLAM approach in [10] consists of a measurement update and a dynamic update. Our approach directly reduces the computational complexity of the measurement update. As our approximation gives rise to sparsity patterns in the map representation, our approximation also gives rise to a reduction in complexity in the dynamic update.

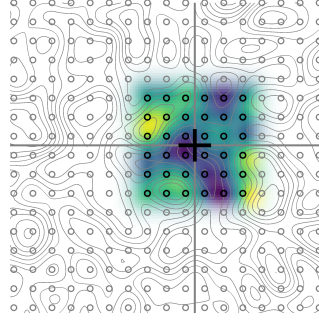


Figure 1: A locally reconstructed approximation (indicated by the color of the heatmap) of a simulated large, nonlinear geospatial field (indicated with gray level curves) based on a local subset (marked with the black circles) of a global grid of basis functions (marked with the gray circles).

The remainder of the paper is organized as follows: Section 1 gives an overview of some background information. Specifically, it introduces GP regression and basis function approximations to GPs. Section 2 gives a description of our method for approximating a large GP scale map, and shows how the map can be incorporated in an EKF for SLAM. Section 3 gives an overview of the relation between our proposed mapping algorithm and other online GP mapping algorithms that can be used in SLAM. Section 4 describes experimental results comparing our proposed approach to other mapping and SLAM algorithms. Section 5 gives some concluding remarks and recommendations for future work.

1 Background

1.1 GP Regression

We are interested in estimating the terrain map using a GP. GP regression allows for estimating a nonlinear function $f : \mathbb{R}^d \rightarrow \mathbb{R}$, distributed according to

$$f \sim \mathcal{GP}(0, \kappa(\cdot, \cdot)), \quad (1)$$

where $\kappa(x, x') : \mathbb{R}^d \times \mathbb{R}^d \rightarrow \mathbb{R}$ is some known kernel function, and $\mathcal{GP}(0, \kappa(\cdot, \cdot))$ denotes the GP prior (see [9] for definition) with a mean of 0 and covariance defined by the kernel function. The kernel that is used for all of the mentioned online GP maps in section 3 is called the squared exponential kernel, and is defined as

$$\kappa_{\text{SE}}(x, x') = \sigma_{\text{SE}}^2 \left(\frac{\|x - x'\|_2^2}{2l_{\text{SE}}^2} \right), \quad (2)$$

where $\|\cdot\|_2$ is the Euclidean norm, σ_{SE} is a hyperparameter indicating the magnitude of the spatial variations and l_{SE} is a hyperparameter indicating the expected lengthscale of the spatial variations [9]. GP regression also uses N noisy measurements of the function $y_{1:N} = \{y_t\}_{t=1}^N$ modelled as

$$y_t = f(x_t) + e_t, \quad e_t \sim \mathcal{N}(0, \sigma_y^2), \quad (3)$$

where $x_{1:N} = \{x_t\}_{t=1}^N$ are known input locations where $x_t \in \mathbb{R}^d$, e_t is a measurement noise, σ_y^2 is the noise variance, and $\mathcal{N}(0, \sigma_y^2)$ denotes the normal distribution with mean 0 and covariance σ_y^2 . The expected value and variance of the function value in any arbitrary location $x^* \in \mathbb{R}^d$ is then given by

$$\begin{aligned} \mathbb{E}[f(x^*)] &= K(x^*, x_{1:N}) (K(x_{1:N}, x_{1:N}) + \sigma_y^2 I_N)^{-1} y_{1:N}, \end{aligned} \quad (4a)$$

$$\begin{aligned} \text{Var}[f(x^*)] &= \\ &= K(x^*, x_{1:N}) (K(x_{1:N}, x_{1:N}) + \sigma_y^2 I_N)^{-1} \\ &= K(x_{1:N}, x^*) + K(x^*, x^*), \end{aligned} \quad (4b)$$

respectively. Here, the matrix $K(x_{1:N}, x_{1:N})$ is constructed by the kernel evaluated along each possible cross-combination of the entries in the vector $x_{1:N}$, such that the entry on the i th row and the j th column of $K(x_{1:N}, x_{1:N})$ is $\kappa(x_i, x_j)$. Similarly, the row vector $K(x^*, x_{1:N})$ is defined such that the j th column is defined by $\kappa(x^*, x_j)$. By the same notation, $K(x^*, x^*)$ is a single-entry matrix with value $\kappa(x^*, x^*)$. We are concerned with approximating the GP posterior. To distinguish the posterior in (4a) and (4b) from any approximation of it, we will refer to this as the full GP posterior. Computing the full GP posterior has a complexity of $\mathcal{O}(N^3)$, as it requires the inversion of a $N \times N$ matrix.

1.2 Sparse approximations to GP Regression with Basis Functions

Sparse approximations to GP regression approximate the function f with a linear combination of m basis functions according to

$$f \approx \Phi^\top w, \quad w \sim \mathcal{N}(0, P), \quad (5)$$

where $w = \{w_i\}_{i=1}^m$ is a set of m scalar weights, and Φ is a vector of m basis functions $\phi_i : \mathbb{R}^d \rightarrow \mathbb{R}$ [11]. The prior covariance on the weights $P \in \mathbb{R}^{m \times m}$ is chosen so that (5) approximates (1) [11].

There are different methods to approximate predictions using the assumption in (5). A commonly used one is the Deterministic Training Conditional (DTC) approximation [11]. The sparse predictions with DTC are given by

$$\mathbb{E}[f(x^*)] \approx \Phi(x^*)^\top (\Phi(x_{1:N})\Phi(x_{1:N})^\top + \sigma_y^2 P^{-1})^{-1} \Phi(x_{1:N})y_{1:N}, \quad (6a)$$

$$\begin{aligned} \text{Var}[f(x^*)] \approx & \sigma_y^2 \Phi(x^*)^\top (\Phi(x_{1:N})\Phi(x_{1:N})^\top + \\ & \sigma_y^2 P^{-1})^{-1} \Phi(x^*) \\ & + K(x^*, x^*) - \Phi(x^*)^\top P \Phi(x^*), \end{aligned} \quad (6b)$$

where the entry on the i th row and the j th column of the matrix $\Phi(x_{1:N})$ is defined as $\phi_i(x_j)$, and the i th row of the column vector $\Phi(x^*)$ is defined as $\phi_i(x^*)$. The expressions in (6a) and (6b) require $\mathcal{O}(Nm^2 + m^3)$ operations to compute, and $\mathcal{O}(Nm^2)$ storage. This greatly improves the computational complexity in the case where the number of basis functions $m \ll N$ compared to the full GP approach in Section 1.1. The required number of basis functions m required to accurately approximate the GP scales with the size of the input domain relative to the lengthscale (l_{SE} in (2)) of the kernel [12].

2 Method

In terrain mapping we typically have large areas and small lengthscales. The approach from Section 1.2 needs many basis functions in this case. To remedy this scaling, we propose training on a large grid of finite-support basis functions which we will introduce in Section 2.1. We incorporate each new measurement with an information filter. Section 2.2 describes how we include a new measurement. Including a new measurement in the way described in section 2.2 has a computational complexity of $\mathcal{O}(m'^2)$, where m' is the number of basis functions with overlapping support in any input location. Section 2.3 describes how we use this trained map to make a prediction. Making a prediction in the way described in Section 2.3 requires $\mathcal{O}(m'^3)$ computations. Section 2.4 suggests how our proposed GP map approximation can be integrated into EKF SLAM with GP maps. The algorithm given in Section 2.4 requires $\mathcal{O}(m)$ computations at each timestep.

2.1 Choice of Basis Functions

We choose a set of basis functions $\{\phi_j\}_{j=1}^m$ as truncated cross-sections with centers distributed on a uniform grid according to

$$\phi_j(x) = \begin{cases} \kappa(u_j, x), & \|x - u_j\|_\infty \leq r \\ 0, & \|x - u_j\|_\infty > r \end{cases}, \quad (7)$$

where $\|\cdot\|_\infty$ denotes the sup-norm, and where each basis function j is centered in a fixed location $u_j \in \mathbb{R}^d$ on a d -dimensional grid. For stationary geospatial fields, d is maximally 3. The basis functions converge to the basis functions induced by a grid of inducing inputs as the truncation limit tends to infinity. A grid of inducing inputs is known to converge to the true GP as the grid density goes to infinity [13].

2.2 Recursive map estimation

Since the basis function approximation in (5) to the full GP regression is a parametric model, the posterior can be found using stochastic least squares estimation. A stochastic least squares estimate can recursively be obtained using an information filter without any dynamics. Specifically, obtaining the posterior on information form corresponds to computing the terms $\Phi(x_{1:N})y_{1:N}$ and $\Phi(x_{1:N})\Phi(x_{1:N})^\top$ in (6a) and (6b) recursively [14]. In the remainder of this paper, we let the information vector at time t be defined as $\iota_{1:t} = \Phi(x_{1:t})y_{1:t}$, and the information matrix at time t be

defined as $\mathcal{I}_{1:t} = \Phi(x_{1:t})\Phi(x_{1:t})^\top$. Updating the information vector $\iota_{1:t}$ and the information matrix $\mathcal{I}_{1:t}$ as [14]

$$\iota_{1:t} = \iota_{1:t-1} + \Phi(x_t)y_t, \quad (8a)$$

$$\mathcal{I}_{1:t} = \mathcal{I}_{1:t-1} + \Phi(x_t)\Phi(x_t)^\top, \quad (8b)$$

only requires updating a finite amount of elements $m' \ll m$ in each update step when using the basis functions from Section 2.1. This is because the terms $\Phi(x_t)y_t$ and $\Phi(x_t)\Phi(x_t)^\top$ only contain m' non-zero elements because only m' basis functions have overlapping support in any given location. The set \mathcal{S} of basis functions (identified by their index j) that are non-zero in x_t follows from the definition of the basis functions in (7) as

$$\mathcal{S} = \{j \mid \|x_t - u_j\|_\infty \leq r\}. \quad (9)$$

It follows that for any single measurement y_t , the only entries of the information vector ι_j that change are the ones where $j \in \mathcal{S}$. Let l_u denote the distance between two neighboring inducing inputs along each dimension. The size of the set \mathcal{S} will always be smaller than or equal to $m' = (\frac{2r}{l_u} + 1)^d$, where d is the dimension of the input vector. The recursive updates in (8a) and (8b) only need to be applied to entries $j \in \mathcal{S}(x_t, r)$ for the information vector, and $j, j' \in \mathcal{S}(x_t, r) \times \mathcal{S}(x_t, r)$ for the information matrix, as the contribution from the term $\phi_j(x_t)y_t$ and $\phi_j(x_t)\phi_{j'}(x_t)$ will be zero for all other entries. Hence this update has computational complexity $\mathcal{O}(m')$ for the information vector, and $\mathcal{O}(m'^2)$ for the information matrix.

2.3 Prediction

Making a prediction of the terrain value in a new location requires evaluating the GP posterior mean and covariance in that location.

We could simply plug the information vector $\iota_{1:N} = \Phi(x_{1:N})y_{1:N}$ and the information matrix $\mathcal{I}_{1:N} = \Phi(x_{1:N})\Phi(x_{1:N})^\top$ into the approximate GP posterior in (6a) and (6b). However, solving these equations would require solving a linear system with m variables, which in general requires $\mathcal{O}(m^3)$ operations. Instead, we use only a local subset of m'' basis functions to perform each prediction. We select the local subset of basis functions in a local domain surrounding the prediction point.

The entries of the information vector of any subset of the basis functions are a subset of the entries of the information vector $\iota_{1:N}$. Equivalently, the entries of the information matrix of any subset of the basis functions are a subset of the entries of the information matrix $\mathcal{I}_{1:N}$. As an illustrating example, consider a set of four basis functions $\{1, 2, 3, 4\}$. Then, consider the subset of basis functions indicated in black $\{2, 3\}$. The entry at row i and column j of the information matrix $\mathcal{I}_{1:N}$ is given by $\mathcal{I}_{1:N}^{i,j} = \sum_{t=1}^N \phi_i(x_t)\phi_j(x_t)$. The entry in row i of the information vector $\iota_{1:N}$ is given by the sum $\iota_{1:N}^i = \sum_{t=1}^N \phi_i(x_t)y_t$. The information matrix and information vector for the full set can therefore be written element-wise as

$$\mathcal{I}_{1:N} = \begin{bmatrix} \mathcal{I}_{1:N}^{1,1} & \mathcal{I}_{1:N}^{1,2} & \mathcal{I}_{1:N}^{1,3} & \mathcal{I}_{1:N}^{1,4} \\ \mathcal{I}_{1:N}^{2,1} & \mathcal{I}_{1:N}^{2,2} & \mathcal{I}_{1:N}^{2,3} & \mathcal{I}_{1:N}^{2,4} \\ \mathcal{I}_{1:N}^{3,1} & \mathcal{I}_{1:N}^{3,2} & \mathcal{I}_{1:N}^{3,3} & \mathcal{I}_{1:N}^{3,4} \\ \mathcal{I}_{1:N}^{4,1} & \mathcal{I}_{1:N}^{4,2} & \mathcal{I}_{1:N}^{4,3} & \mathcal{I}_{1:N}^{4,4} \end{bmatrix}, \quad (10a)$$

$$\iota_{1:N} = [\iota_{1:N}^1 \quad \iota_{1:N}^2 \quad \iota_{1:N}^3 \quad \iota_{1:N}^4]. \quad (10b)$$

The information matrix and information vector of basis functions 2 and 3 is a subset of the information matrix and information vector indicated by the black sub-entries in (10a)-(10b).

We leverage this property to define an approximation to the GP based on a local subset S^* of basis functions close to the prediction point. In Fig. 1 we illustrate how a local subset of basis functions can be selected from a global grid. The local subset of the corresponding information vector and information matrix defined as $\iota_{1:N}^* = \Phi_{S^*}(x_{1:N})y_{1:N}$ and $\mathcal{I}_{1:N}^* = \Phi_{S^*}(x_{1:N})\Phi_{S^*}(x_{1:N})^\top$, respectively, can be constructed from subsets of the information vector $\iota_{1:N}$ and the information matrix $\mathcal{I}_{1:N}$ for the full grid. From acquiring the information matrix and information vector on the global grid of basis functions indicated with gray circles in Fig. 1, we have access to the trained system the local subsets of basis functions illustrated with black circles in Fig. 1.

Formally, we choose $S^* = S(x^*, r^*)$ consisting of all basis functions whose center is closer than r^* along each dimension to be in this set. The size of the set $S(x^*, r^*)$ will always be smaller than or equal to $m'' = (\frac{2r^*}{l_u} + 1)^d$, where d is the dimension of the input vector. Evaluating the predicted mean and predicted variance using the basis

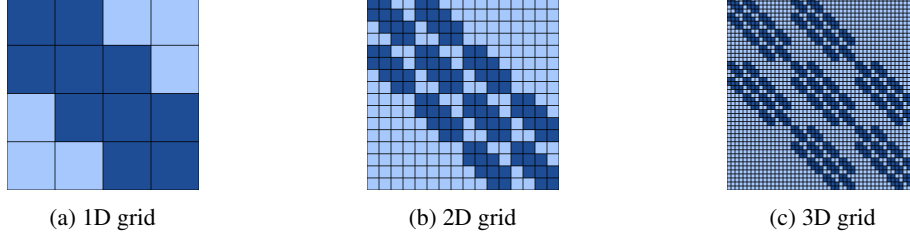


Figure 2: Sparsity patterns illustrating which entries i, j in the information matrix correspond to pairs of basis function locations x_i, x_j that are closer than $2r^*$ according to the infinity norm (dark blue) and which are not (light blue). The patterns arise from the ordering of the indexes of the basis functions, relative to their locations along each of the three dimensions.

functions indexed by the set S^* in place of the basis functions $\{1, \dots, N\}$ in (6a)-(6b) gives

$$\mathbb{E}[f(x^*)] \approx \Phi_{S^*}(x^*)^\top (\mathcal{I}_{1:N} + \sigma_y^2 P_\star^{-1})^{-1} \iota_{S^*}, \quad (11a)$$

$$\begin{aligned} \text{Var}[f(x^*)] &\approx \sigma_y^2 \Phi_{S^*}(x^*)^\top (\mathcal{I}_{1:N} + \sigma_y^2 P_\star^{-1})^{-1} \\ &\quad \Phi_{S^*}(x^*) + K(x^*, x^*) \\ &\quad - \Phi_{S^*}(x^*)^\top P_\star \Phi_{S^*}(x^*), \end{aligned} \quad (11b)$$

where the i th row and the j th column of $\Phi_{S^*}(x^*)$ is defined by the evaluation of basis functions number i in the subset S^* on the prediction point x^* , and where P_\star is the prior covariance on the basis function weights. We select P_\star such that the prior is recovered exactly in the center locations u_{S^*} of the basis functions, which gives $P_\star = (\Phi_{S^*}(u_{S^*}))^{-\top} K(u_{S^*}, u_{S^*}) (\Phi_{S^*}(u_{S^*}))^{-1}$. A detailed derivation for the expression for P_\star is given in Appendix ?? . As the size m'' of the set S^* is always smaller than or equal to $(\frac{2r^*}{l_u} + 1)^d$, the matrix inversion required in (11a) and (11b) is bounded. The prediction of our proposed GP prediction in (11a)-(11b) can therefore be computed with $\mathcal{O}(m''^3) = \mathcal{O}((\frac{2r^*}{l_u} + 1)^{3d})$ operations.

2.4 Integration of mapping algorithm into an EKF for magnetic field SLAM

In this section, we give the algorithmic details of the implementation of a SLAM algorithm with an EKF as it is described in [10], but using our proposed map approximation instead of Hilbert space basis functions. From here on we will refer to the magnetic field SLAM algorithm with and EKF in [10] as EKF Mag-SLAM.

EKF Mag-SLAM gives estimates of the sensor's position \hat{x}_t , its orientation $\hat{q}_{t|t}$ and the magnetic field map $\hat{m}_{t|t}$. The magnetic field map is parameterized as the estimate of the weights w_t of a sparse GP approximated with Hilbert space basis functions, using online measurements of the magnetic field denoted y_t at each timestep t and measurements of the change in position and orientation denoted Δq_t and Δp_t at each timestep t respectively.

We use the same measurement and dynamic model as [10] (see Eqns (14a), (14b) and (13)), but we replace the basis functions denoted Φ with the finite-support basis functions described in section 2.1. As the computational benefits of the finite-support basis functions arise on the information form, we implement the EKF on the information form.

In the measurement update, the system is approximated using only the information of the basis functions that are closer than r^* to the prediction point. This means that the information between two prediction points that are further apart than $2r^*$ will never be needed to carry out the measurement update. This means that the only entries of the information matrix we need to compute to carry out the dynamic update are given a sparse subset of the information matrix. We name this subset of all index pairs such that the distance between the corresponding basis functions is less than $2r^*$ as $S_{v^*} = \{i, j \mid \|x_i - x_j\|_\infty \leq 2r^*\}$. The location of the indices corresponding to this subset for the information matrix for Mag-SLAM in three dimensions is illustrated in Fig. 2. The pattern arises from the ordering of the indices in the information matrix according to the location of the finite-support basis functions along each of the three spatial dimensions.

As the information matrix for online Kalman filters with dynamic updates [15] is generally defined as the inverse of the covariance matrix P , we initialize the information matrix as $I_0^{\text{EKF}} = P_0^{-1}$. Comparing this information matrix to the one defined generally in The initial error state of EKF Mag-SLAM is zero and thus the initial information vector $\iota_0 = \mathcal{I}_0^{\text{EKF}} \xi_0 = 0$.

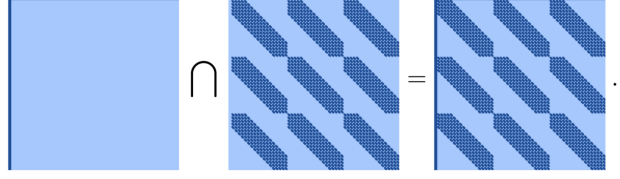


Figure 3: Sparsity pattern illustration of the information matrix for the full state consisting of the position, orientation and magnetic field. The first sparsity pattern has a dark blue color in the entries corresponding to the first six columns and the first six rows of the information matrix (corresponding to position and orientation), and a light blue color in the other entries. The second sparsity pattern has a dark blue color in the entries in the set $S_{\forall \star}$ of all entries that can possibly be necessary to make a map prediction in any location. The last sparsity pattern is the union of these two sets.

The dynamic update on information form in general is given by

$$\mathcal{I}_{t+1}^{\text{EKF}} = (\mathcal{I}_t^{\text{EKF}} + Q)^{-1} \quad (12)$$

Where Q is the process noise on the state-space vector, defined in equation (23) in [10]. Since we assume the map to be static, the matrix Q can be factorized according to

$$\begin{bmatrix} \tilde{Q} & 0 \\ 0 & 0 \end{bmatrix} = V^\top Q V, \quad V = [I \quad 0], \quad (13)$$

and where \tilde{Q} is a 6×6 matrix expressing the process noise on the position and orientation. After applying the matrix inversion lemma to this dynamic update, it reduces to

$$\mathcal{I}_{t+1}^{\text{EKF}} = \mathcal{I}_t^{\text{EKF}} - \mathcal{I}_t^{\text{EKF}} V^\top (V \mathcal{I}_t^{\text{EKF}} V^\top + \tilde{Q})^{-1} V \mathcal{I}_t^{\text{EKF}}. \quad (14)$$

The Kalman filter measurement update of the information matrix when applied to Mag-SLAM becomes [15]

$$\mathcal{I}_{t+1}^{\text{EKF}} = \mathcal{I}_t^{\text{EKF}} + \frac{1}{\sigma_y^2} H_t H_t^\top, \quad (15)$$

where the Jacobian of the measurement model H_t is as derived in a similar way as equation (25) in [10], but with finite-support basis functions from 7 replacing the Hilbert space basis functions. This update, as the one in (8b) is inherently sparse, and has complexity $O(m'')$. Similarly, the information vector of EKF-Mag SLAM at each timestep becomes [15]

$$l_t^{\text{EKF}} = \frac{1}{\sigma_y^2} H_t y_t, \quad (16)$$

with y_t being a three-component magnetic field measurement. (see [16] for a detailed derivation of the extended information filter). The re-linearisation of the estimated position, orientation and magnetic field would then in general require an inversion of the full information matrix. However, by employing the approximation that only the basis functions that are closer to the prediction point (which in this case is the estimated location) are the ones necessary to approximate the magnetic field, we can execute the re-linearisation at a computational cost of $\mathcal{O}(m''^3)$. We do this explicitly according to

$$\begin{bmatrix} \delta_t^\top & \eta_t^\top & \nu_{\star,t}^\top \end{bmatrix}^\top = (I_{t,\star}^{\text{EKF}})^{-1} l_{t,\star}^{\text{EKF}}, \quad (17a)$$

$$\hat{p}_{t|t} = \hat{p}_{t|t-1} + \delta_t, \quad (17b)$$

$$\hat{q}_{t|t} = \hat{q}_{t|t-1} \odot \exp_q(\eta_t), \quad (17c)$$

$$\hat{m}_{\star,t|t} = \hat{m}_{\star,t|t-1} + \nu_{\star,t}, \quad (17d)$$

where we only add the correction on the linearisation point corresponding to the magnetic field map m_t in the entries in the subset S_\star . The orientation estimate $\hat{q}_{t|t}$ is represented as a unit quaternion. The operator $\exp_q(\cdot)$ is defined in [17].

What is worth noting about the relinearisation in equation (17) is that it only requires knowledge of a subset S_\star of the entries in the information matrix. Furthermore, for all possible position estimates $\hat{p}_{t|t-1} \in \mathbb{R}^3$, the union of all possible subsets S_\star is given as the set of index pairs i, j where the corresponding basis functions are closer to each other according to the infinity norm than $2r^\star$. We can formally define this union of all possible usable subsets as $S_{\star,\forall} = \{i, j \mid \|p_{i,t} - p_{j,t}\|_\infty \leq 2r^\star\}$. For an information matrix I , this subset is a sparse subset of the full set of entries, with $\mathcal{O}(mm''^2)$ elements. Assuming $m \gg m''$, this sparse subset contains $\mathcal{O}(m)$ elements. Fig. 2 illustrates examples of sparsity patterns for an information matrix corresponding to a one-dimensional, a two-dimensional, and a

three-dimensional grid of equispaced basis functions. In the one-dimensional grid, four basis functions are located along the x-axis at $[-1.5, -0.5, 0.5, 1.5]$, and the indexes are ordered correspondingly in Fig. 2. In the two-dimensional grid, 16 basis functions are located along the x and y-axis at

$$\begin{bmatrix} -1.5 & -1.5 & -1.5 & \dots & 1.5 & 1.5 \\ -1.5 & -0.5 & 0.5 & \dots & 0.5 & 1.5 \end{bmatrix}, \quad (18)$$

and also indexed chronologically.

The only entries of the information matrix that are used to compute the term $\mathcal{I}^{\text{EKF}}V^\top(V\mathcal{I}^{\text{EKF}}V^\top + \tilde{Q})^{-1}V\mathcal{I}^{\text{EKF}}$ are the entries in the first 6 rows and the first 6 columns of the information matrix. These are the only entries that can possibly affect the values contained in $\mathcal{S}_{\forall \star}$ during the dynamic update. The only entries of the information matrix we need to keep track of are therefore the union of the first 6 columns and the first 6 rows and the values in $\mathcal{S}_{\forall \star}$. Fig. 3 shows an example of the union of these two sparsity sets, for our estimation problem with an equispaced 3D grid of finite-support basis functions. The sparsity pattern shows a fractal-like structure that is explained by the fact that we are displaying the pattern for a 3D grid of basis functions, and the nature of the ordering of the indexes of these basis functions. It is therefore sufficient during application of the entire algorithm to only keep track of the entries in $\mathcal{S}_{\forall \star}$, and in the first six rows and the first six columns.

3 Relation to existing work

Many approximations to GP maps have been proposed to remedy the poor scalability of GP terrain maps. The particular use-case our proposed approximation does well compared to previous work is the ability to perform online GP mapping with a computational complexity that does not change over time as more measurements are gathered (temporal scalability), and that simultaneously does get slower as the size of the map increases relative to the spatial variations (spatial scalability).

3.1 Temporally scalable approaches which are not spatially scalable

GP regression approximated with basis functions is a temporally scalable and well-established strategy for online GP mapping [18, 4, 10, 19, 20, 2]. This is commonly used for online learning with GP regression [21]. A prediction can also be made at any time in any location with a computational complexity of $\mathcal{O}(m^2)$.

Practical examples of realistic terrains used for aiding navigation have small spatial variations relative to the size of the map [22, 23, 24, 25]. Existing sparse approximations to GPs with basis functions require a number of computations which scale with the size of the mapped area relative to the lengthscale of the kernel [26]. This is due to the fact that GP approximations that efficiently recover the higher eigenvalues of the kernel but not the smaller eigenvalues will, in general, have poor performance when the lengthscale of the kernel is small relative to the domain [26, 12]. In practice, this manifests as a need for a larger number m of basis functions as the domain size increases [12], which in turn increases the computational requirements $\mathcal{O}(m^2)$. Another online GP mapping approximation using finite-support basis functions was proposed by [27], which uses a sparse-weight Kalman filter for this approach as described in [28], and therefore has a computational complexity of including each new measurement of $\mathcal{O}(m)$.

In both our work and a range of other work, the magnetic field map is estimated online in a Bayesian filter for SLAM by including the basis function weights in the state space [2, 4, 10]. Basis-function approximation to GPs are employed for online creation of magnetic field maps [4], underwater bathymetry maps [2] and ground elevation maps [18]. Due to the computational cost of $\mathcal{O}(m^2)$, SLAM algorithms using basis function approximations to create the map are limited to a small map area [2, 10, 19], or to breaking up the map into separate maps without sharing information between the maps [4, 29].

3.2 Spatially scalable approaches which are not temporally scalable

There is also some work for large-scale terrain mapping that suggests using only the k nearest measurements for applying GP regression [30, 23]. This approach uses KD-trees for efficient querying of the data. It requires storage which scales linearly in the amount of measurements. The storage requirements of this approach will therefore increase over time. Although they are spatially scalable, these approximations are therefore not spatially scalable.

3.3 Spatially and temporally scalable approximations that suffer from boundary effects

Local GPs avoid the issues of increased computational complexity with increasing domain size by splitting the input domain into discrete sub-domains [31, 32]. This approach suffers from discontinuities and inaccurate predictions at the

domain boundaries [31]. Patched local GPs [33] and domain decomposition methods [34] both remedy this problem by introducing constraints connecting the local domains. However, this remedy to the boundary effect problem requires a number of computations that scale with the number of considered domains and thus do not truly achieve a prediction time complexity independent of the spatial size of nonlinear field [33]. Although all of the previously mentioned local GP regression approximations are formulated offline, an online approach to local GP regression was proposed by [35].

The technique of splitting the field into sub-domains have also been integrated into SLAM [5, 4, 36]. These approaches often require additional modifications in the SLAM algorithm to handle the cases where position estimates are close to borders of the domains, where the boundary effects are strong [4]. This is in contrast to our proposed approach, where the local domain always surrounds the prediction point, and therefore does not suffer from boundary effects.

3.4 Structured Kernel Interpolation

Another approximation that performs GP regression efficiently in large maps was proposed by [37]. It applies the Woodbury matrix inversion lemma to reduce the required computational complexity of a GP approximation called Structured Kernel Interpolation (SKI) [13]. SKI uses grid-structured finite-support basis functions to perform approximate GP regression.

The novelty in our contribution in contrast to SKI is that we perform these updates online and that we perform predictions using only a local subset of m'' of the finite support basis functions. The prediction cost of [37] is dependent on the size of the input domain. Each prediction with SKI, therefore, requires $\mathcal{O}(m \log(m))$ operations, while each prediction with our method requires only $\mathcal{O}(m''^3)$ operations. SKI therefore is able to include new measurements in the map in a way which is both spatially and temporally scalable. In contrast to our work, SKI requires more computations to make predictions as the size of the map area grows. A detailed comparison of the computational complexity of SKI and our approach is given in table 1.

Table 1: Comparison of computational complexities for online mapping.

Step	(SKI, [37])	Our method	HS functions
Meas update	$\mathcal{O}(m'^2)$	$\mathcal{O}(m'^2)$	$\mathcal{O}(m^2)$
Prediction	$\mathcal{O}(m \log(m))$	$\mathcal{O}(m''^3)$	$\mathcal{O}(m)$

3.5 Integration into SLAM

The use of our approximation reduces the overall computational complexity of an existing extended Kalman filter Mag-SLAM (EKF-Mag-SLAM) algorithm with Hilbert space basis functions [10]. Mag-SLAM with an EKF or requires a measurement update and dynamic update at each timestep. Additionally, a prediction of the magnetic field is required at each timestep (this is officially part of the measurement update, but we consider it a separate step to evaluate the computational complexity required to make this prediction). Incorporating our approach in Mag-SLAM gives direct improvements to the computational requirements for the measurement update, and for making a prediction. Furthermore, our approximation of using only a local subset of the basis functions in the prediction step induces a sparsity structure which reduces the computational requirements of the dynamic update. This causes an overall improved computational complexity of the EKF Mag-SLAM algorithm in [10] to reduce from $\mathcal{O}(m^2)$ to $\mathcal{O}(m)$. An overview of the computational complexities of EKF Mag-SLAM with our mapping technique compared to EKF Mag-SLAM with Hilbert space methods is given in table 2.

Table 2: Comparison of computational complexities after integrating the approach into SLAM.

Step	EKF	EKF
	Mag-SLAM with our method	Mag-SLAM with HS functions
Meas update	$\mathcal{O}(m'^2)$	$\mathcal{O}(m^2)$
Prediction	$\mathcal{O}(m''^3)$	$\mathcal{O}(m)$
Dyn update	$\mathcal{O}(m)$	$\mathcal{O}(m^2)$

4 Results

In this section, we first compare the performance of our method with existing approaches on two low-dimensional, spatially large benchmark data sets. As the choice of kernel hyperparameters affects the trade-off between computational

Table 3: SMAE accuracies, combined time to include a new measurement and make a new prediction, MSLL scores on audio dataset. The results that obtain the lowest run-time while also obtaining the lowest SMAE is highlighted. SMAEs and MSLL scores are evaluated on all standardized test points inside the considered domain, and the average time plus minus one standard deviation is calculated based on 100 repetitions.

	10% of domain, $m = 800$			100% of domain, $m = 8000$		
	SMAE	Time[s]	MSLL	SMAE	Time[s]	MSLL
$r = 6l_{SE}$	0.42	$6.2 \cdot 10^{-5} \pm 2.1 \cdot 10^{-5}$	37.5	0.34	$7.3 \cdot 10^{-5} \pm 2.2 \cdot 10^{-5}$	48.0
$r = 12l_{SE}$	0.22	$9.4 \cdot 10^{-5} \pm 2.1 \cdot 10^{-5}$	4.18	0.20	$1.1 \cdot 10^{-4} \pm 1.6 \cdot 10^{-5}$	12.2
$r = 18l_{SE}$	0.22	$1.3 \cdot 10^{-4} \pm 2.7 \cdot 10^{-5}$	3.94	0.20	$1.6 \cdot 10^{-4} \pm 2.1 \cdot 10^{-5}$	12.2
SKI	0.22	$8.0 \cdot 10^{-4} \pm 1.2 \cdot 10^{-4}$	5.74	0.20	$1.6 \cdot 10^{-3} \pm 1.7 \cdot 10^{-4}$	18.2
Inducing inputs	0.22	$1.0 \cdot 10^{-2} \pm 7.4 \cdot 10^{-4}$	3.81	0.20	$2.1 \cdot 10^{-1} \pm 1.6 \cdot 10^{-3}$	12.2
Hilbert space	0.22	$9.5 \cdot 10^{-3} \pm 5.1 \cdot 10^{-4}$	3.80	0.20	$2.2 \cdot 10^{-1} \pm 4.6 \cdot 10^{-3}$	12.2

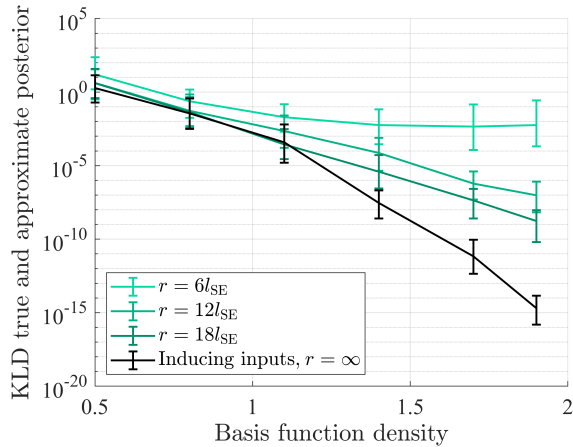


Figure 4: KL divergence (KLD) between the full GP posterior, and approximations with various local domain sizes r , trained on the audio dataset. The error bars indicate the average deviation above and below the mean, respectively, after 100 repeated experiments with 100 randomly sampled measurements from the training set.

complexity and the approximation accuracy, to ensure a fair comparison, we consider the same hyperparameters that are used by previous work for these data sets. See [13, 37] for the audio dataset, and [37, 38] for the precipitation dataset. Then, we measure how long it takes for our method to make online predictions using a short length scale and millions of basis functions on a bathymetry dataset that is too large for existing approaches given our hardware constraints. For the experiments we perform on the audio benchmark, like other approaches that use this dataset as a benchmark to investigate spatial scalability [13, 37], we treat the temporal axis as a spatial axis.

As the data sets considered in Sections 4.2 and 4.3 are geospatial data with a non-zero mean value, the average of the output is subtracted before training. This average is subsequently added to each prediction. All computation times reported are measured while running on a Dell XPS 15 9560 laptop, with 16 GB RAM and an Intel Core i7-7700HQ CPU running at 2.80 GHz. In all experiments we set $r = 2r^*$, as picking $r \geq 2r^*$ gives that the expression for P_\star^{-1} reduces to $P_\star^{-1} = K(u_{S^\star}, u_{S^\star})$, as derived in Appendix ???. This means that we have a closed-form expression for the inverse of the prior covariance which does not rely upon computing any numerical inverses, further reducing the necessary computational efforts to make each prediction. All predictions are made using the squared exponential kernel. All code and files required to reproduce the results can be found on <https://github.com/fridaviset/FastGPMapping>.

4.1 One-dimensional sound map

A dataset describing natural sound was published by [39], and subsequently used by [13] and [37] to demonstrate the ability of their approximations to learn a large dataset with a large input domain relative to the size of the spatial variations in the field. This section describes various experiments that all make a one-dimensional GP map from the time axis to the amplitude of the sound wave.

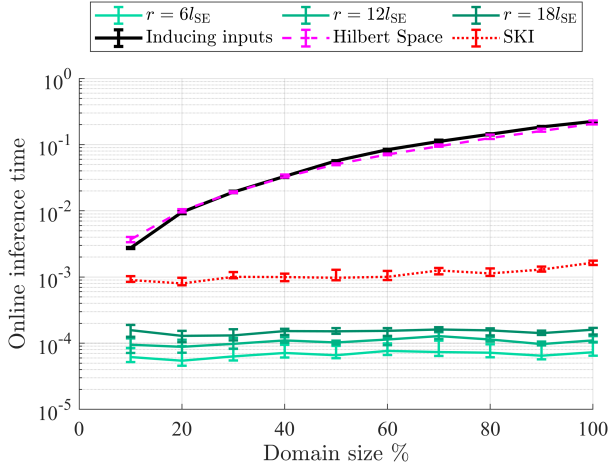


Figure 5: Online inference time on audio dataset for a growing domain size for our proposed method with various local domain sizes r , compared to the inducing input approximation using inducing inputs on a grid, the Hilbert space basis function approximation, and SKI. All methods were run using the same amount of basis functions. The error bars indicate the average deviation above and below the mean after 100 repeated experiments, respectively.

We illustrate multiple properties of our approximation using this dataset. Firstly, we show on the audio dataset that our approximation converges to the inducing point approximation as the radius of the local domain increases. Secondly, we show that our approach converges to the GP posterior as both the radius of the local domain and the basis function density increase. Thirdly, we show that our approach has a lower online computation time compared to both SKI, inducing points, and Hilbert space methods on the full dataset while matching the prediction accuracy measured by SMAE.

To evaluate the accuracy and required computation time on the same dataset with the same GP prior as [37], we use the squared exponential kernel in equation 2 with hyperparameters set to $\sigma_{SE} = 0.009$, $l_{SE} = 10.895$, $\sigma_y = 0.002$. The dataset is one-dimensional and contains a training set of 59 309 measurements of sound amplitude collected at a known input time and a fixed test set of 691 points.

In Fig. 4 we investigate how high the grid density has to be for the basis function approximation described in section 1.2 using the basis functions described in section 2.1 with $r = \infty$ and for our proposed method in sections 2.2 and 2.3 with various local domain sizes r . We assess our results in terms of the KL divergence between the approximate inference and the full GP posterior. This is a measure that can attain values between 0 and ∞ that compares how similar distributions are and a lower value means that the distributions are more similar. For all the investigated approximations, a higher basis functions density (measured in the number of basis functions per lengthscale) gives a lower KL divergence between the approximate inference and the full GP posterior. The results demonstrate that the KL divergence between the full GP posterior and our approximation reduces with increasing parameter choice r .

To measure how long it takes for our approach to perform online mapping, we measure the time it takes to include one additional measurement and perform one prediction step. In Fig. 5, we compare our proposed method to the inducing input solution implemented with an online Kalman filter [21], an online Kalman filter implementation with Hilbert space basis functions [12], and an online implementation of SKI [37], for increasing domain sizes. As the domain size increases, we keep the basis function density constant to retain the same approximation accuracy. The amount of basis functions m is therefore increasing linearly. As the online inference time of SKI is affected by how many iterations are used in the conjugate gradient solver to improve the approximation accuracy, we measure the run-time using just one iteration in the solver. To compare the prediction accuracy of SKI to our approach in Table 3, however, we use the exact solution that the solver is approximating. We can therefore conclude that an online evaluation of our algorithm is faster than competing approaches while being able to recover the same or better SMAE (standardized mean average error) and MSLL (mean squared log loss) scores (see Table 3). The online computational complexity of both Hilbert space basis functions and inducing inputs increases quadratically as the domain size increases. The computational complexity of our approach is bounded by $O(m^3)$ independent of the increase in the domain size, which is why our online computational complexity remains lower than 10^{-3} seconds independent of the growth of the domain size.

Table 4: SMSE accuracies of daily precipitation level predictions. The predictions are obtained with a local domain with size $r^* = 3l_{SE}$, which corresponds to using at most 144 basis functions in each local prediction for the highest $m = 800K$.

N	full GP	Inducing inputs			Local information filter		
10 000	0.823	0.957	0.905	0.957	0.906	0.824	0.823
20 000	0.766	0.946	0.861	0.947	0.862	0.770	0.766
100 000	N/A	0.907	0.782	0.907	0.786	0.561	0.545
528 474	N/A	0.894	0.746	0.895	0.751	0.468	0.435

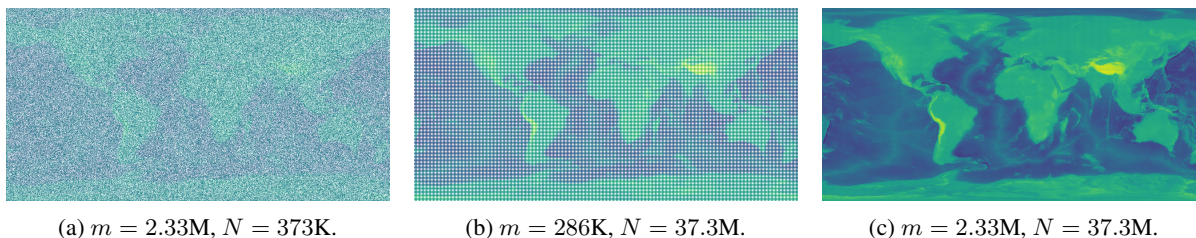


Figure 6: Bathymetry dataset reconstruction with GP regression. The color corresponds to the posterior predicted elevation of the earth surface both above and below the sea, and the opacity is inversely proportional to the variance of the approximate GP prediction in each location.

4.2 Mapping daily precipitation levels

In this section, we compare the prediction accuracy and computation time of our mapping approach to alternative methods on a large geo-spatial dataset which is used as a benchmark dataset for evaluation accuracy and computation time by [37], and [13].

The precipitation dataset contains 528 474 measurements of daily precipitations from the US in the training set, and 100 000 measurements in the test set [37]. The input dimensions are latitude, longitude, and time. We use the squared exponential kernel using the same hyperparameters as [37]. These hyperparameters are $\sigma_{SE} = 3.99$, $\sigma_y = 2.789$ and $l_{SE} = [3.094, 2.030, 0.189]$, where the three lengthscales l_{SE} apply to each of the three dimensions, respectively. The results are displayed in Table 4.

In Table 4, the standardized mean squared error (SMSE) of our approach with $r^* = 3.5l_{SE}$ is compared to the full GP prediction, and to the inducing input approximation with basis functions placed on the same grid. The SMSE of our approach almost matches the inducing input approximation with the same number of basis functions. Using 800 000 basis functions, it matches the GP prediction accuracy with the same number of measurements. Using all the measurements and 800 000 basis functions gives the highest prediction accuracy, which is a combination that is computationally infeasible given our hardware constraints for both the full GP regression and the inducing input approximation to give a prediction. However, our proposed method has an online training time of 0.017 seconds per measurement and 0.016 seconds per prediction.

4.3 Global Bathymetry Field Mapping

To investigate the time required for our method to include a new measurement and make a prediction in a large geospatial field with fine-scale variations, we run it on a dataset containing values of the height difference with respect to sea level across the globe [40]. The input domain of this data is huge compared to the scale of the spatial variations, and the data is therefore challenging to train on using state-of-the-art methods. We retrieve 37.5 million depth values from the database, and we consider the latitude and longitude as input locations.

We test our approach with the hyperparameters σ_{SE}^2 equal to the variance of the 37.5 million measurements, $\sigma_y = 0.1\sigma_{SE}$, and a lengthscale $l_{SE} = 0.16$ degrees (which corresponds to 18.3 km on the equator). We use a local subset contained within $r^* = 3l_{SE}$ for our prediction-point dependent local approximations to the GP posterior mean. We perform predictions using our proposed algorithm for three cases: one where we use 2.33 million basis functions and 373 thousand measurements, one where we use 268 thousand basis functions and 37.3 million measurements, and one where we use both 2.33 million basis functions and 37.3 million measurements.

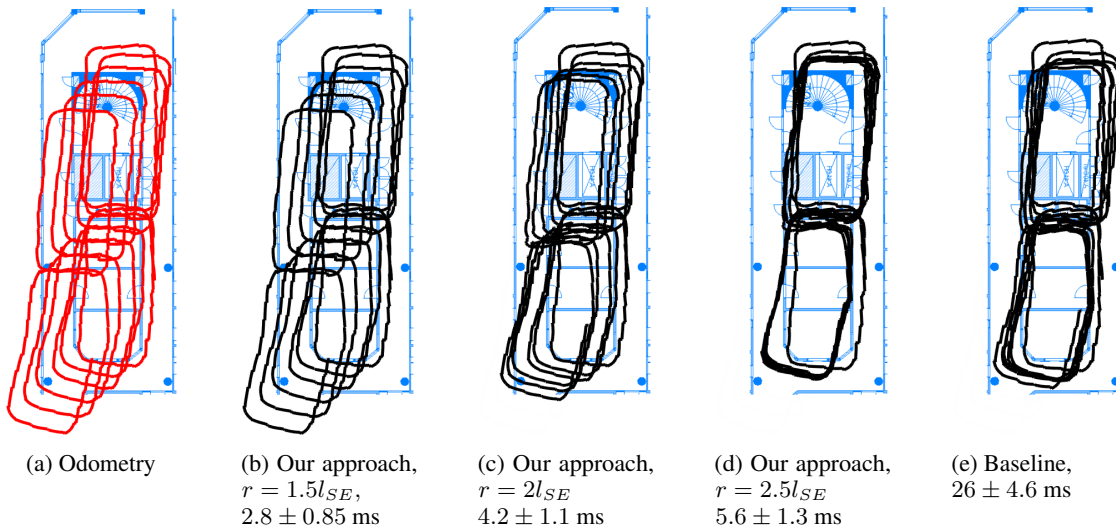


Figure 7: Trajectory estimates for indoor pedestrian walking laps in a hallway using only foot-mounted odometry, EKF-SLAM with the local information filter with various sizes of the local domain determined by r and EKF-SLAM with Hilbert space basis function (baseline). The average computation time in milliseconds for one iteration of each filter (dynamic update + measurement update) is written below each sub-Fig..

The result in Fig. 6 shows the learned bathymetry map using 10% of the measurements, and 2.33 million basis functions (Fig. 6a), and the learned map using 100% of the measurements and 268 thousand measurements (Fig. 6b) with a map learned with 100% of the measurements and a dense grid of 2.33 million basis functions (Fig. 6c). For the results in Fig. 6c, including each new measurement takes $3.7 \times 10^{-4} \pm 0.12 \times 10^{-4}$ seconds. Each prediction takes 0.0097 ± 0.017 seconds. These results demonstrate that our proposed approach can remain computationally feasible in cases where the measurement density is high, and the map area is large relative to the length scale of the spatial variations. For that particular usecase, our proposed approach does not have the disadvantage of discarding measurements which is visible in Fig. 6a, which is that some areas can be far from any measurements relative to the lengthscale of the inference, meaning that the prediction in some areas is less certain than in others. Similarly, our proposed approach does not have the disadvantage of using less tight grids of inducing points, which is visible in Fig. 6b, where the prediction points far from inducing point locations are less certain than the ones close to the inducing point locations.

4.4 Using local information filter for faster Mag-SLAM

To experimentally compare the local information filter with Hilbert space basis functions in EKF Mag-SLAM, we apply both algorithms to a dataset from a foot-mounted sensor that was collected by [41] and subsequently used in [10] to demonstrate the drift-compensating abilities of EKF Mag-SLAM. We replace the Hilbert space basis function approximation with the local basis function approximation in EKF Mag-SLAM as described in section 2.4, and measure the average computation time required to make each iteration of the algorithm on the same laptop computer. We compare this with the average computation time required to make each iteration of the original EKF Mag-SLAM using Hilbert space basis functions.

In Fig. 7a, the odometry obtained by using only accelerometer and gyroscope measurements from a foot-mounted sensor using the algorithm in [42] is displayed. In Fig. 7e, the estimated trajectory using the EKF with Hilbert space basis functions as in [10] is displayed. All estimates are overlaid the floorplan of the building where the measurements were collected. This gives a rudimentary means of evaluating the position estimation accuracy, since the subject was repeatedly walking through the same hallways in a repeated pattern 8-motion. The drift in the odometry in Fig. 7a therefore shows up as a slow displacement of the position estimate away from the hallway the pedestrian was walking in. In contrast, the estimates obtained from our approximate mapping in Fig. 7d and from the baseline EKF Mag-SLAM with Hilbert space basis functions in Fig. 7e compensate for the drift of the estimates from the gyroscope and accelerometer. The notable difference between our approach and the approximation using Hilbert space functions, is that the Hilbert space basis functions require 26 ± 4.6 ms to run at each iteration, while our equally accurate algorithm require 5.6 ± 1.3 ms to run at each iteration.

5 Conclusion

To improve indoor position estimates online with few computational resources, we have presented an efficient online mapping technique that gives an approximation to the GP posterior requiring a number of computations that neither scales with the temporal duration of the mapping, nor with the spatial extent of the map. The storage requirements of our presented mapping algorithm scales linearly with the spatial extent of the map, and does not scale with the temporal duration of the mapping. We have also demonstrated the ability of our mapping algorithm to match the accuracy of previously proposed approximations on benchmark datasets using a lower computation time. It is possible to replace a previously proposed GP approximation in an EKF for Mag-SLAM. Our experiments on data from a foot-mounted sensor using our proposed method achieve the same prediction accuracy as Mag-SLAM with a previously proposed mapping approximation using a shorter computation time on the same computer. Future work could investigate the existence of theoretical bounds on the approximation errors, or investigate ways to incorporate the mapping technique for SLAM in different geospatial fields, and for other applications such as navigation of robots or vehicles.

References

- [1] Jongdae Jung, Seung-Mok Lee, and Hyun Myung. Indoor Mobile Robot Localization and Mapping Based on Ambient Magnetic Fields and Aiding Radio Sources. *IEEE Transactions on Instrumentation and Measurement*, 64(7):1922–1934, July 2015. Conference Name: IEEE Transactions on Instrumentation and Measurement.
- [2] Ignacio Torroba, Marco Cella, Aldo Terán, Niklas Rolleberg, and John Folkesson. Online Stochastic Variational Gaussian Process Mapping for Large-Scale Bathymetric SLAM in Real Time. *IEEE Robotics and Automation Letters*, 8(6):3150–3157, June 2023. Conference Name: IEEE Robotics and Automation Letters.
- [3] Youngjoo Kim and Hyochoong Bang. Utilization of terrain elevation map in SLAM for unmanned aircraft. In *2015 6th International Conference on Automation, Robotics and Applications (ICARA)*, pages 57–62, February 2015.
- [4] Manon Kok and Arno Solin. Scalable Magnetic Field SLAM in 3D Using Gaussian Process Maps. In *2018 21st International Conference on Information Fusion (FUSION)*, pages 1353–1360, July 2018.
- [5] Patrick Robertson, Martin Frassl, Michael Angermann, Marek Doniec, Brian J. Julian, Maria Garcia Puyol, Mohammed Khider, Michael Lichtenstern, and Luigi Bruno. Simultaneous Localization and Mapping for pedestrians using distortions of the local magnetic field intensity in large indoor environments. In *proceedings of the International Conference on Indoor Positioning and Indoor Navigation*, pages 1–10, October 2013.
- [6] S. Barkby, S. B. Williams, O. Pizarro, and M. V. Jakuba. Bathymetric SLAM with no map overlap using Gaussian Processes. *Proceedings of the International Conference on Intelligent Robots and Systems*, pages 1242–1248, September 2011. Conference Name: 2011 IEEE/RSJ International Conference on Intelligent Robots and Systems (IROS 2011) ISBN: 9781612844565 9781612844541 9781612844558 Place: San Francisco, CA Publisher: IEEE.
- [7] Morten Kjaergaard, Enis Bayramoglu, Alessandro S. Massaro, and Kjeld Jensen. Terrain Mapping and Obstacle Detection Using Gaussian Processes. In *Proceedings of the 10th International Conference on Machine Learning and Applications and Workshops*, volume 1, pages 118–123, December 2011.
- [8] Hyeonwoo Yu and Beomhee Lee. Terrain field SLAM and Uncertainty Mapping using Gaussian Process. In *Proceedings of the 18th International Conference on Control, Automation and Systems (ICCAS)*, pages 1077–1080, October 2018.
- [9] Carl Edward Rasmussen and Christopher K. I. Williams. *Gaussian Processes for Machine Learning*. The MIT Press, November 2005.
- [10] Frida Viset, Rudy Helmons, and Manon Kok. An Extended Kalman Filter for Magnetic Field SLAM Using Gaussian Process Regression. *Sensors*, 22(8):2833, January 2022. Number: 8 Publisher: Multidisciplinary Digital Publishing Institute.
- [11] Joaquin Quiñero-Candela and Carl Edward Rasmussen. A Unifying View of Sparse Approximate Gaussian Process Regression. *The Journal of Machine Learning Research*, 6:1939–1959, December 2005.
- [12] Arno Solin and Simo Särkkä. Hilbert Space Methods for Reduced-Rank Gaussian Process Regression. *Statistics and Computing*, January 2014.
- [13] Andrew Wilson and Hannes Nickisch. Kernel interpolation for scalable structured gaussian processes (KISS-GP). In Francis Bach and David Blei, editors, *Proceedings of the 32nd International Conference on Machine Learning*, volume 37 of *Proceedings of machine learning research*, pages 1775–1784, Lille, France, July 2015. PMLR.

- [14] Arthur G. O. Mutambara. *Decentralized Estimation and Control for Multisensor Systems*. CRC Press, January 1998. Google-Books-ID: Z1YfUGkG8poC.
- [15] Matthew R. Walter, Ryan M. Eustice, and John J. Leonard. Exactly Sparse Extended Information Filters for Feature-based SLAM. *The International Journal of Robotics Research*, 26(4):335–359, April 2007.
- [16] Sebastian Thrun, Daphne Koller, Zoubin Ghahramani, Hugh Durrant-Whyte, and Andrew Y. Ng. Simultaneous Mapping and Localization with Sparse Extended Information Filters: Theory and Initial Results. In Jean-Daniel Boissonnat, Joel Burdick, Ken Goldberg, and Seth Hutchinson, editors, *Algorithmic Foundations of Robotics V*, Springer Tracts in Advanced Robotics, pages 363–380. Springer, Berlin, Heidelberg, 2004.
- [17] Manon Kok, Jeroen Hol, and Thomas Schön. *Using Inertial Sensors for Position and Orientation Estimation*. Now Foundations and Trends, January 2017.
- [18] Alberto Viseras, Thomas Wiedemann, Christoph Manss, Lukas Magel, Joachim Mueller, Dmitriy Shutin, and Luis Merino. Decentralized multi-agent exploration with online-learning of Gaussian processes. In *proceedings of the International Conference on Robotics and Automation (ICRA)*, pages 4222–4229, May 2016.
- [19] Dohyun Jang, Jaehyun Yoo, Clark Youngdong Son, Dabin Kim, and H. Jin Kim. Multi-Robot Active Sensing and Environmental Model Learning With Distributed Gaussian Process. *IEEE Robotics and Automation Letters*, 5(4):5905–5912, October 2020. Conference Name: IEEE Robotics and Automation Letters.
- [20] Frida Viset, Jan Tommy Gravdahl, and Manon Kok. Magnetic field norm SLAM using Gaussian process regression in foot-mounted sensors. In *proceedings of the European Control Conference (ECC)*, pages 392–398, Delft, Netherlands, June 2021. IEEE.
- [21] Hildo Bijl, Jan-Willem van Wingerden, Thomas B. Schön, and Michel Verhaegen. Online sparse Gaussian process regression using FITC and PITC approximations. *IFAC-PapersOnLine*, 48(28):703–708, January 2015.
- [22] R. Karlsson and F. Gustafsson. Bayesian Surface and Underwater Navigation. *IEEE Transactions on Signal Processing*, 54(11):4204–4213, November 2006. Conference Name: IEEE Transactions on Signal Processing.
- [23] Shrihari Vasudevan, Fabio Ramos, Eric Nettleton, Hugh Durrant-Whyte, and Allan Blair. Gaussian Process modeling of large scale terrain. In *Proceedings of International Conference on Robotics and Automation*, pages 1047–1053, May 2009. ISSN: 1050-4729.
- [24] Petr Tichavský, Ondřej Straka, and Jindřich Duňík. Grid-Based Bayesian Filters With Functional Decomposition of Transient Density. *IEEE Transactions on Signal Processing*, 71:92–104, 2023. Conference Name: IEEE Transactions on Signal Processing.
- [25] F. Gustafsson, F. Gunnarsson, N. Bergman, U. Forssell, J. Jansson, R. Karlsson, and P.-J. Nordlund. Particle filters for positioning, navigation, and tracking. *IEEE Transactions on Signal Processing*, 50(2):425–437, 2002.
- [26] Yi Ding, Risi Kondor, and Jonathan Eskreis-Winkler. Multiresolution Kernel Approximation for Gaussian Process Regression. In *Advances in Neural Information Processing Systems*, volume 30. Curran Associates, Inc., 2017.
- [27] Anton Kullberg, Isaac Skog, and Gustaf Hendeby. Online Joint State Inference and Learning of Partially Unknown State-Space Models. *IEEE Transactions on Signal Processing*, 69:4149–4161, 2021. arXiv: 2102.07418.
- [28] Simon Julier and LaViola Jr. On Kalman Filter With Nonlinear Equality Constraints. *Signal Processing, IEEE Transactions on*, 55:2774 – 2784, July 2007.
- [29] Frida Viset, Rudy Helmons, and Manon Kok. Distributed multi-agent magnetic field norm SLAM with Gaussian processes. In *2023 26th International Conference on Information Fusion (FUSION)*, pages 1–8, June 2023.
- [30] Ilari Vallivaara, Janne Haverinen, Anssi Kemppainen, and Juha Röning. Magnetic field-based SLAM method for solving the localization problem in mobile robot floor-cleaning task. In *proceedings of the 15th International Conference on Advanced Robotics (ICAR)*, pages 198–203, June 2011.
- [31] Robert B. Gramacy and Daniel W. Apley. Local Gaussian Process Approximation for Large Computer Experiments. *Journal of Computational and Graphical Statistics*, 24(2):561–578, 2015. Publisher: [American Statistical Association, Taylor & Francis, Ltd., Institute of Mathematical Statistics, Interface Foundation of America].
- [32] Edward Snelson and Zoubin Ghahramani. Local and global sparse Gaussian process approximations. In *Proceedings of the Eleventh International Conference on Artificial Intelligence and Statistics*, pages 524–531. PMLR, March 2007. ISSN: 1938-7228.
- [33] Chiwoo Park and Jianhua Z. Huang. Efficient Computation of Gaussian Process Regression for Large Spatial Data Sets by Patching Local Gaussian Processes. *Journal of Machine Learning Research*, 17(174):1–29, 2016.
- [34] Chiwoo Park, Jianhua Z. Huang, and Yu Ding. Domain Decomposition Approach for Fast Gaussian Process Regression of Large Spatial Data Sets. *Journal of Machine Learning Research*, 12(47):1697–1728, 2011.

- [35] Duy Nguyen-tuong, Jan Peters, and Matthias Seeger. Local Gaussian Process Regression for Real Time Online Model Learning. In *Advances in Neural Information Processing Systems*, volume 21. Curran Associates, Inc., 2008.
- [36] Mostafa Osman, Frida Viset, and Manon Kok. Indoor SLAM using a foot-mounted IMU and the local magnetic field. In *proceedings of the 25th International Conference on Information Fusion (FUSION)*, pages 1–7, July 2022.
- [37] Mohit Yadav, Daniel Sheldon, and Cameron Musco. Faster Kernel Interpolation for Gaussian Processes. In *Proceedings of The 24th International Conference on Artificial Intelligence and Statistics*, pages 2971–2979. PMLR, March 2021. ISSN: 2640-3498.
- [38] Kun Dong, David Eriksson, Hannes Nickisch, David Bindel, and Andrew G Wilson. Scalable Log Determinants for Gaussian Process Kernel Learning. In *Advances in Neural Information Processing Systems*, volume 30. Curran Associates, Inc., 2017.
- [39] Richard E Turner. *Statistical Models for Natural Sounds*. PhD thesis, Gatsby Computational Neuroscience Unit, UCL, 2010.
- [40] {GEBCO Compilation Group}. Gridded bathymetry data GEBCO (General Bathymetric Chart of the Oceans) 2021 Grid., 2021.
- [41] Isaac Skog. OpenShoe Matlab Framework, 2012. Publication Title: OpenShoe - Foot-mounted INS for every foot.
- [42] Isaac Skog, John-Olof Nilsson, Peter Händel, and Arye Nehorai. Inertial Sensor Arrays, Maximum Likelihood, and Cramer-Rao Bound. *IEEE Transactions on Signal Processing*, 64:1–1, August 2016.